

## EDGE DEGREE-OF-SHARPNESS AND INTEGRAL LENGTH SCALE EFFECTS ON THE AERODYNAMICS OF A BRIDGE DECK

Luca Bruno\* and Davide Fransos†

\*Dipartimento di Ingegneria Strutturale e Geotecnica  
Politecnico di Torino, Viale Mattioli 39, 10126 Torino, Italy  
e-mail: luca.bruno@polito.it

†Dipartimento di Matematica  
Politecnico di Torino, Corso Duca degli Abruzzi 24, 10126 Torino, Italy  
e-mail: davide.fransos@polito.it

**Keywords:** Bridge deck, degree of sharpness, turbulence integral length scale, aerodynamic regimes, Computational Wind Engineering

**Abstract:** *This paper discusses the sensitivity of the aerodynamic behaviour of a trapezoidal-shaped bridge deck cross-section to its lower corner degree-of-sharpness and to the incoming flow turbulence integral length scale in conjunction with low turbulence intensity. Since these features are hard to set and measure in experimental facilities, the aerodynamic behaviour of the body has been investigated through the computational simulation of the flow around it. The results are given in term of force coefficients, Strouhal number, pressure distribution along its surface, and the mean and instantaneous flow patterns. Dramatic changes in the force coefficients and Strouhal number occur following small changes in the parameters' values. These changes have been found to be due to significant modifications in the topological structure of the flow. Special emphasis has been given to the analysis of the separation and reattachment points, the recirculation bubble length, the vortex shedding mechanisms and the wake structures. On the basis of the obtained results, four aerodynamic regimes have been pointed out in analogy with the well-known individual Re number regimes. Some of these regimes have also been recognized on the Sunshine Skyway Bridge cross-section, even when the sharpening aerodynamic devices at the lower corners are taken into consideration.*

## 1 Introduction

Aerodynamic similarity in experimental studies is a key element in the evaluation of wind forces acting on civil engineering structures. A lack of aerodynamic similarity between the prototype and the experimental conditions can result from discrepancies in the incoming flow, in the wind tunnel scaled model dimensions and in the wind-tunnel or computational model shape details. These discrepancies can be hard to quantify, because real-world conditions are affected by uncertainties and the worst-case scenario cannot be designed *a priori*, and/or because it is difficult to set and measure some experimental set-up characteristics.

The effects of various incoming flow parameters on bluff body aerodynamics has attracted the attention of the scientific community since the milestone works by Delany and Sorensen [2] and Roshko [12] concerning Reynolds number effects on circular cylinders and on rounded-edge cylinders (radius-to-width ratio  $R/D = 0.02, 0.083, 0.167, 0.25, 0.333, 0.5$ ) of various shapes. The work by Roshko introduced the well known nomenclature for the individual Re number regimes of circular cylinders. Later on, pronounced Reynolds number effects were observed by Schewe and Larsen [14] in the aerodynamic behaviour of slender bodies with sharp edged cross sections such as bridge box girders.

Analogous fundamental studies evaluated the effects of free-stream turbulence features on the separated and reattaching flow past the sharp edge of rectangular plates, starting with the pioneering work of Laneville and Williams [4] and going on to those of Nakamura and Ozono [10] and Li and Melbourne [6]. The above mentioned works, in particular, placed emphasis on the turbulence scale effects on the separation bubble past the leading edge of elongated plates and on the interaction with vortex shedding from compact bluff bodies. A discontinuous sensitivity of the mean streamwise surface pressure to turbulence scale was recognized for wide ranges of scales at turbulence intensities of more than 10%. More recently, Tamura and Miyagi [15] have focused on the combined effects of turbulence intensity and corner shape (sharp corners, chamfered and rounded edges  $R/D = 0.167$ ) on the overall aerodynamics forces acting on a square cylinder.

A significant generalization effort was made by Schewe [13] who reviewed the Re number effects on the flow around several more-or-less bluff bodies. The individual Re number regimes proposed by Roshko were generalized for a wide ranges of bodies, regardless of their specific geometry. The location of laminar-to-turbulent transition was suspected to be the key element that drives the boundary layer separation, its possible reattachment and the wake topology, and could therefore be assumed as the main phenomenological-based classifying criterion. Larose and D'Auteuil [5] have reviewed recent cases of real structures, mainly bridge decks, where Reynolds number effects have been depicted. They also made an attempt to identify some parameters that sensitize bluff bodies with sharp edges to Re effects, and chose rectangular prisms as a benchmark. In particular, they chose the turbulence intensity, the chord-to-width  $B/D$  ratio and the edge treatments, i.e. small and large chamfers ( $R/D = 0.04, 0.125$ , respectively).

The conceptual framework of this work suggests that the generalized individual Re number regimes proposed by Schewe [13] are not bounded by fixed Re watershed values, but the latter can be modified by each flow and/or obstacle feature that affects boundary layer separation and reattachment. As an extreme case, several regimes can take place at the same Re number, provided the boundary layer separation and reattachment around a given bluff body show significant sensitivity to the other flow features.

The present work aims at offering a contribution to verify this conceptual outcome. Two experimental condition related parameters have been retained for the sensitivity study, that

characterize both the incoming flow and the obstacle geometry. The combined effects of the turbulence integral length scale ( $1e-3 \leq Lt/B \leq 1$ ) at low turbulence intensity ( $It = 1\%$ ) and of the lower corner small radius of curvature ( $0.01 \leq R/B \leq 0.05$ ) on the flow field around a trapezoidal bridge deck cross-section have been systematically addressed. These parameters were chosen for three main reasons.

First, they are expected to have significant effects on separated and reattaching flows around bluff bodies, coherently with what was identified by Larose and D’Auteuil [5].

Second, the chosen ranges cover the “grey zone” between smooth and turbulent incoming flow conditions and between sharp and rounded bluff bodies, respectively. Significant difficulties in fact remain in experimental studies on the aerodynamic effects of the small edge radius of curvature and integral length scales at low turbulence intensity, because of the restrictions in wind tunnel practice concerning physical model manufacturing and free-stream velocity measurements. The purpose of the present paper is to tackle such difficulties by means of a computational approach that allows the turbulent incoming flow characteristics to be set and the smallest obstacle geometrical features to be described in order to evaluate the body aerodynamic behaviour under uncommon, or even experimentally unrealizable, physical states.

Finally, a significant sensitivity to these parameters was suspected for an actual long-span bridge deck. The sensitivity study was therefore applied to the trapezoidal bare deck cross section of the cable-stayed Sunshine Skyway Bridge (Figure 1), which is characterized by a  $B/D = 6.41$ . Previous experimental and computational studies reported in Ricciardelli and

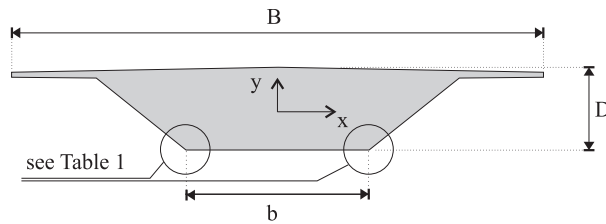


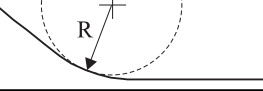


Figure 1: Bare Sunshine Skyway Bridge deck cross section

Hangan [11], Mannini [7] and Mannini et al. [9] showed in fact that the lower corner smoothing and sharpening dramatically affects the force coefficients and Strouhal number  $St_D$  (Table 1). The deck section is in particular subjected to an upwards mean lift coefficient  $\overline{C}_L$  in conjunction with sharp corners and to a downwards one when the edges are rounded. Both wind tunnel test setups were characterized by the same Reynolds number  $Re_B = 3 \div 6e + 5$  order of magnitude, the same null angle of attack and low turbulence incoming flow, i.e.  $It \leq 1\%$ , while the turbulence integral length scale  $Lt$  was not reported in the cited works. The model tested by Ricciardelli and Hangan [11] was equipped by sharpening aerodynamic appendages at the lower edges, while the one used by Mannini [7] was characterized by rounded lower corners due to the alloy folded plate manufacturing process. The spanwise averaged radius-to-chord ratio was estimated by Mannini [8] to be equal to  $R/B = 0.05$ . Previous computational simulations performed by Mannini et al. [9] showed that the discrepancies in experimental results could be ascribed to two different body wake topologies that take place for sharp (curvature radius  $R/B = 0$ ) and rounded ( $R/B = 0.05$ ) lower corners.

Table 1: Experimental and computational results in literature

	$St_D$	$\overline{C}_L$	corner
Wind tunnel [11, $It \leq 1\%$ ]	0.146	0.294	
Computational [9, smooth flow]	0.154	0.288	
Wind tunnel [7, $It \leq 1\%$ ]	0.210	-0.189	
Computational [9, smooth flow]	0.255	-0.022	

## 2 Modelling and computational approach

The incompressible, turbulent, separated, unsteady flow around the 2D section is modelled by the classical Time-dependent Reynolds Averaged Navier-Stokes (T-RANS) equations, which, in Cartesian coordinates, read:

$$\frac{\partial \overline{u}_i}{\partial x_i} = 0 \quad (1)$$

$$\frac{\partial \overline{u}_i}{\partial t} + \overline{u}_j \frac{\partial \overline{u}_i}{\partial x_j} = -\frac{1}{\rho} \frac{\partial \overline{p}}{\partial x_i} + \frac{\partial}{\partial x_j} \left[ \nu \left( \frac{\partial \overline{u}_i}{\partial x_j} + \frac{\partial \overline{u}_j}{\partial x_i} \right) \right] - \frac{\partial}{\partial x_j} (\overline{u'_i u'_j}), \quad (2)$$

where  $\overline{u}_i$  is the averaged velocity,  $u'$  the velocity fluctuating component,  $\overline{p}$  the averaged pressure,  $\rho$  the air density and  $\nu$  the air kinematic viscosity. The modified  $k - \omega$  turbulence model proposed by Wilcox [16] is used to close the T-RANS equations:

$$\frac{\partial k}{\partial t} + \overline{u}_i \frac{\partial k}{\partial x_i} = \frac{\partial}{\partial x_i} \left[ \left( \sigma^* \nu_t + \nu \right) \frac{\partial k}{\partial x_i} \right] + P_k - \beta^* k \omega, \quad (3)$$

$$\frac{\partial \omega}{\partial t} + \overline{u}_i \frac{\partial \omega}{\partial x_i} = \frac{\partial}{\partial x_i} \left[ \left( \sigma \nu_t + \nu \right) \frac{\partial \omega}{\partial x_i} \right] + \alpha \frac{\omega}{k} P_k - \beta \omega^2, \quad (4)$$

where  $k$  is the turbulent kinetic energy,  $\omega$  its specific dissipation rate and  $\nu_t = k/\omega$  the so-called turbulent kinematic viscosity. The production term  $P_k$  is modelled through the classic Boussinesq hypothesis:

$$P_k \approx 2\nu_t D_{ij} \frac{\partial \overline{u}_i}{\partial x_j}.$$

The semi-empirical closure coefficients are determined to be:

$$\alpha = 13/25, \quad \beta = 9/125, \quad \beta^* = 9/100, \quad \sigma = 1/2, \quad \sigma^* = 1/2.$$

The low Reynolds number  $k$  one-equation model (Two-Layer Model) proposed by Chen and Patel [1] is adopted in the viscosity-affected near-wall region  $Re_y = \sqrt{k}y/\nu \leq 200$ , where  $y$  is the normal distance from the wall at the cell centre. The turbulent viscosity  $\nu_t$  and the specific dissipation rate  $\omega$  are obtained using the solved turbulent kinetic energy  $k$  from the relations:

$$\nu_t = C_\mu \sqrt{k} l_\mu, \quad \omega = \frac{k^{1/2}}{l_\varepsilon},$$

where  $C_\mu = 0.09$  is a dimensionless constant. The length scales  $l_\mu$  and  $l_\varepsilon$  are expressed by the following relations:

$$l_\mu = c_l y \left[ 1 - \exp\left(-\frac{Re_y}{A_\mu}\right) \right], \quad l_\varepsilon = c_l y \left[ 1 - \exp\left(-\frac{Re_y}{A_\varepsilon}\right) \right], \quad (5)$$

where the semi-empirical values of the constants are:

$$c_l = k C_\mu^{-3/4}, \quad A_\mu = 70, \quad A_\varepsilon = 2c_l.$$

The extension of the computational domain in space and the conditions applied at its outer boundaries are depicted in Figure 2. Dirichlet conditions on the velocity field and on the turbu-

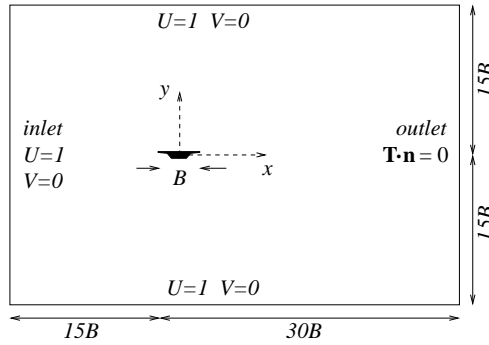


Figure 2: Analytical domain and boundary conditions

lence characteristic quantities ( $k$  and  $\omega$ ) are imposed at the inlet boundaries. Neumann conditions involving the velocity field and the pressure (null normal component of the stress tensor) as well as the same Dirichlet conditions on  $k$  and  $\omega$  are imposed at the outlet boundaries. No-slip conditions are imposed at the deck section surface. Impulsive initial conditions are introduced.

A hybrid quadrilateral/triangular grid is employed in space. A body-fitted, structured quadrangular grid is generated near the obstacle wall in order to guarantee the best grid quality with orthogonal and unskewed cells. The cell thickness close to the wall is set equal to  $y_w = 5.e-6B$  in order to accurately resolve the turbulent wall boundary layer, as confirmed by an obtained non dimensional wall unit averaged value  $y^+ = 0.4$  at the Reynolds number of interest.

Even though the accurate simulation of the flow in the wall neighbourhood plays a dominant role in predicting boundary layer separation/reattachment and vortex shedding mechanisms, an analogous precision is required to predict the velocity distribution in the wake in order to correctly simulate the vortex transport mechanisms. Hence, special attention is devoted to the computational grid quality and density in the near wake, according to the grid convergence study performed by Fransos and Bruno [3]. The region down-wind to the trailing edge is meshed by a structured cartesian quadrangular grid characterized by a constant non-dimensional cv surface approximately equal to  $A_{cv}/B^2 = 1.e-4$ . The cross-wind dimension  $t_w$  of the refined rectangular sub-domain down-wind to the trailing edge is kept equal to  $B$  while its along-wind extension  $l_w$  is set equal to  $8B$ . The intermediate part of the computational domain is covered by an unstructured triangular grid and the remaining outer part is covered by a coarse structured grid. The computational grid in space consists of about  $2.43e+5$  cells. Uniform impulsive initial conditions are imposed according to the inlet boundary ones.

Each simulation extends in time along 60 nondimensional time units in order to overcome

the transient solution due to impulsive initial conditions and to allow the statistic analysis of the subsequent periodic flow. The nondimensional timestep needed for an accurate advancement in time is  $\Delta t = 0.01$ .

The Finite Volume solver Fluent is used to numerically evaluate the flowfield. The cell-centre values of the variables are interpolated at face locations using a second-order Central Difference Scheme for the diffusive terms on all the elements and Quadratic Upwind Interpolation for Convective Kinematics and second-order Upwind Scheme for the convection terms on quadrilateral and triangular cells, respectively. Advancement in time is accomplished by the second-order implicit Euler scheme.

The computations are carried out on a single Intel Xeon X5355 2.66GHz CPU with 2GB of memory and they require about 60 hours of CPU time for each simulation.

### 3 Application to bare deck section

The geometry of the investigated deck section is the same as in Figure 1 and the lower corner curvature radius  $R$  is defined as in Table 1. No aerodynamic appendages or platform equipment are included in the model. For the sake of simplicity, the dimensionless parameters  $R/B$  and  $Lt/B$  are hereafter notated as  $R$  and  $Lt$ , respectively. It is worth recalling that their investigated values range in the  $0.01 \leq R \leq 0.05$  and  $1e - 3 \leq Lt \leq 1$  intervals. The Reynolds number is kept constant and equal to  $Re_B = 5.76e + 5$  for each simulation, the isotropic turbulence intensity  $It = 1\%$  and the angle of attack  $\alpha = 0$ .

#### 3.1 $R$ - $Lt$ sensitivity analysis

Figure 3 shows performed computational experiment grid in the  $R - Lt$  plane. A total number of 137 computational simulations have been performed, corresponding to about 8220 hours of CPU time. The point density has been adapted step-by-step during the study in order to properly describe the local trend of the most significant aerodynamic integral quantities. The

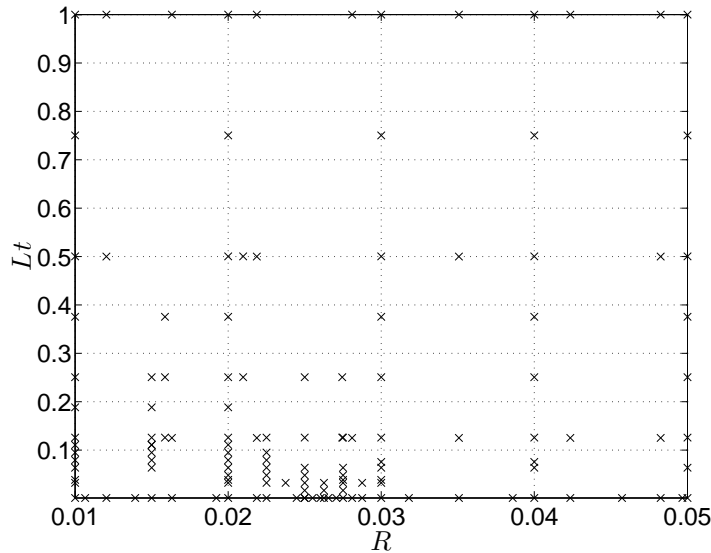


Figure 3: Grid of the computational experiments

Strouhal number  $St_D$  and the mean and rms values of the drag and lift coefficients are in particular selected. The  $St_D$  number is obtained by the Power Spectral Density (PSD) heuristic

analysis of the flow velocity at the near wake point  $x/B = 2.5, y/B = 0$ . The point-wise obtained results and their best piece-wise polynomial least-square fitting are plotted in Figure 4. Four main regions of the investigated  $R - Lt$  plane can easily be distinguished, where some common features can be recognized in the trend of each quantity.

Strong gradients occur for low values of both the curvature radius and the integral turbulence length scale, while smoother variations generally occur at high  $Lt$  values. A sudden drop in the mean aerodynamic forces and a corresponding sudden increase in the  $St$  number occur at the lowest  $Lt = 1.e - 3$  for increasing radius values. The lift coefficient changes in sign, passing from  $\overline{C_L} = +0.25$  to  $\overline{C_L} = -0.1$ , while the  $St$  number passes from  $St_D = 0.16$  to  $St_D = 0.27$ : these results are in good qualitative agreement with the ones reported in previous studies and which are summarized in Table 1. The flow is suspected to be highly unsteady, as the high rms values of the aerodynamic coefficients suggest. The watershed value at which such sudden changes take place has been localized in the narrow  $0.02447 \leq R \leq 0.02499$  range in conjunction with the adopted flow features. The previously mentioned discontinuity would seem to suggest a switch in the overall aerodynamic regime, analogously to what happens in the individual  $Re$  critical regime.

In the intermediate turbulence scale range ( $0.18 \leq Lt \leq 0.3$ ), the flow appears quasi steady in conjunction with low radius values ( $R \leq 0.023$ ), since the drag and lift rms values are almost null.

The  $R$  sensitivity pointed out at low  $Lt$  values dramatically reduces at high turbulence scales ( $Lt \geq 0.3$ ), where each integral parameter is almost constant when  $R$  is varied. Conversely, the  $Lt$  sensitivity still remains at high  $R$  values, even though smoother variations occur, for each integral parameter, than at low  $R$  values. The first outcome is consistent with what is generally stated about the regularizing and smoothing effect of the incoming turbulence intensity on bluff body aerodynamic behaviour. The second one reveals two qualitatively different  $Lt$  sensitivities, i.e. a discontinuous one and a smooth one, for bodies characterized by high and low degree-of-bluffness, respectively.

### 3.2 Aerodynamic regime identification

The trend of the selected integral parameters suggests the necessity of deeply investigating the existence of multiple aerodynamic regimes in the  $R - Lt$  plane for the same  $Re$  number. The computational approach post-processing facilities allow a deeper insight into the mean and instantaneous flow field around the body. Figure 5 shows the time-averaged x-velocity  $u_1$  isocontours corresponding to null and 0.99 nondimensional values, i.e., it points out the reversed and disturbed flow outer boundaries, respectively. Four  $R - Lt$  couples of values are selected to examine the flow features corresponding to the regions mentioned in the previous section. The first and the third cases correspond to the lowest  $Lt = 1e - 3$  value while  $R$  values are chosen to be lower and higher than the watershed value at which discontinuity takes place; the second one is characterized by an  $Lt$  in the intermediate range  $0.1 \leq Lt \leq 0.2$  and by low  $R$ ; the last one corresponds to the highest  $Lt = 1$  value.

Four regimes are identified and named according to the nomenclature adopted by Schewe [13] concerning the  $Re$  effects on a trapezoidal deck because of the analogous observed aerodynamic behaviour. The regimes clearly differ from each other in the position along the upper and lower deck surfaces at which the boundary layer separates and reattaches, as depicted in Figure 5(a) by circles and triangles, respectively:

- sub-critical regime (low  $St$ , high mean and rms drag and lift values), long separation

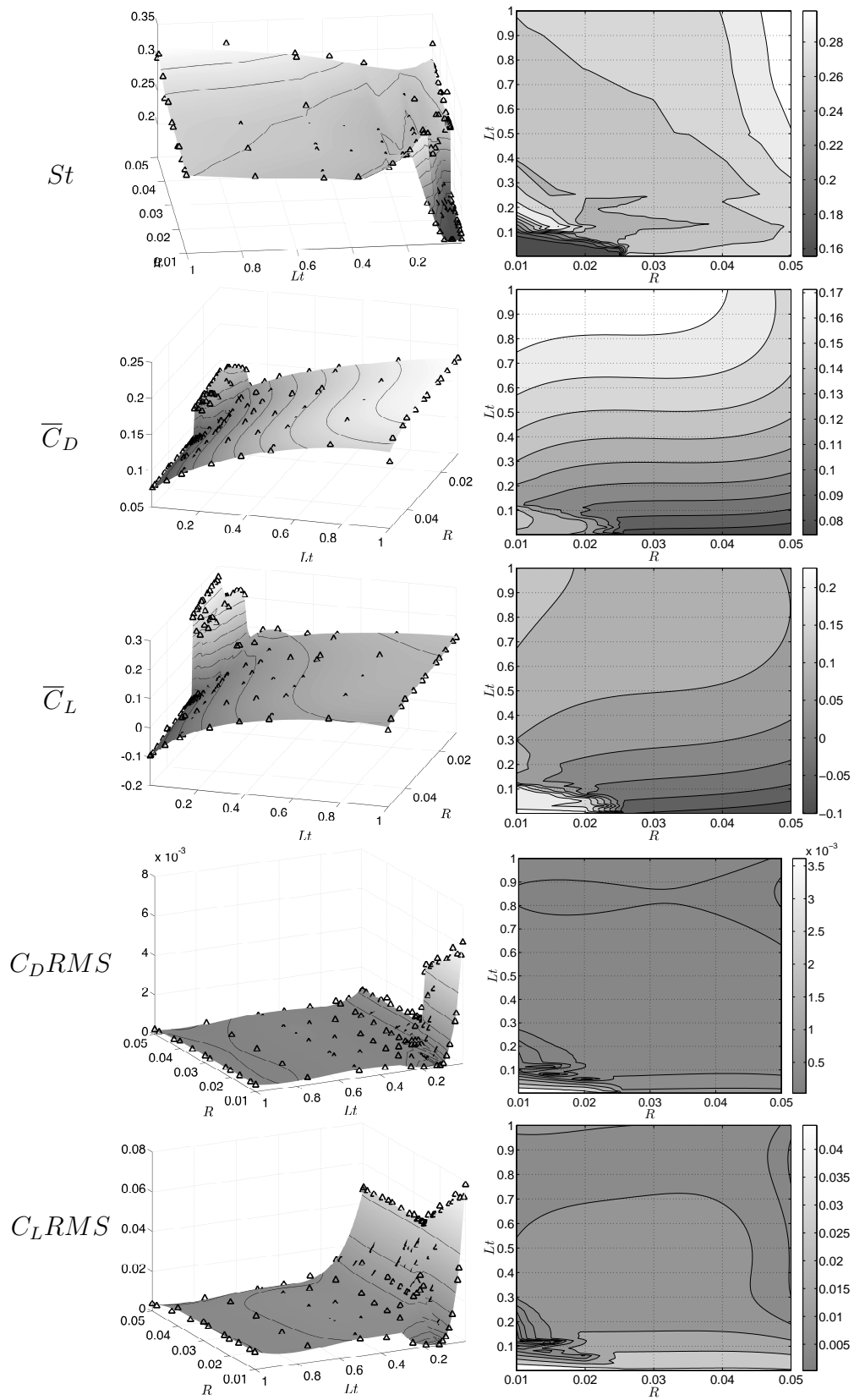


Figure 4: Trend of the aerodynamic coefficients



bubble at the upper surface, separated flow at the lower surface without reattachment;

- critical regime (large variations of the  $St$  number and of the mean drag and lift coefficients, almost null rms values), short separation bubble at the upper surface, long separation bubble at the lower surface due to boundary layer reattachment along the flat plate;
- super-critical regime (high  $St$ , low mean drag and lift values), short separation bubble at the upper surface, the boundary layer separation at the lower surface occurs at the trailing rounded edge;
- trans-critical regime (high  $St$ , high mean and low rms drag and lift values), the boundary layer separation at both the lower and upper surfaces occurs at the trailing edges.

Generally speaking, it is worth pointing out that local changes in the lower edge radius of curvature  $R$  involve not only local effects on the lower surface separation bubble, but also non local ones on the upper surface separation bubble, on the vortex shedding mechanism and finally on the overall aerodynamic deck behaviour.

The near wake mean crosswind extension significantly varies in the four regimes, as shown in Figure 5(b). This flow feature, in conjunction with the large Stouhal number variations, suggests that different vortex shedding mechanisms occur in the identified regimes. The mean and rms x-velocity profiles along the  $x/B = 0.55$  and  $x/B = 1.0$  straights (see Figure 5(b)) are plotted in Figure 6. The mean x-velocity profile points out slight differences in both the maximum velocity defect and its location along the reference straights. In particular, the massive separation at the lower surface in the sub-critical regime drops the maximum velocity defect abscissa below  $y = 0$ . The rms x-velocity profile along the  $x/B = 0.55$  straight reveals dramatic differences in the fluctuating flow field for the regimes: the sub-critical and the super-critical ones show two local peaks, the trans-critical one is characterized by only one peak in correspondence to the upper trailing edge, while the critical one involves negligible x-velocity fluctuations just downwind to the upper trailing edge. In the critical regime, the x-velocity fluctuations develop more downwind to the upper trailing edge, as shown in the rms x-velocity profile along the  $x/B = 1.0$  straight. A more evident physical meaning of the above described profiles is provided in Figure 7, where the instantaneous vorticity magnitude isocontours corresponding to local maxima in the  $C_L$  time history are plotted for the four regimes. The relative distance between two successive vortices shed by the same edge  $\mathcal{L} \propto St^{-1}$  is depicted.

The vortex shedding mechanism mainly distinguishes two classes of regimes. On one hand, the sub and super-critical ones, i.e., the ones defined for a low turbulence length scale, are characterized by vortex shedding from both the upper and lower edges. Nevertheless, it is worth recalling that vortices at the lower surface are shed at the leading edge in the sub-critical regime, while vortex shedding from the trailing edge takes place in the super-critical regime. On the other hand, the critical and trans-critical regimes only involve significant vortex shedding from the upper trailing edge. Nevertheless, the point at which the upper vortices are shed in the wake is more downwind located in the critical regime rather than in the trans-critical one. It is worth pointing out that the  $x/B = 0.55$  straight is upwind to the vortex shedding point in the critical regime, so that the extremely low values in the x-velocity rms profile (Figure 6) are justified. Bearing in mind that vortices are shed downwind in the wake in the critical regime, their contribution to the aerodynamic force fluctuating component is expected to be small in the critical regime. This flow feature can help explain the almost null lift and drag rms values in this regime (Figure 4).

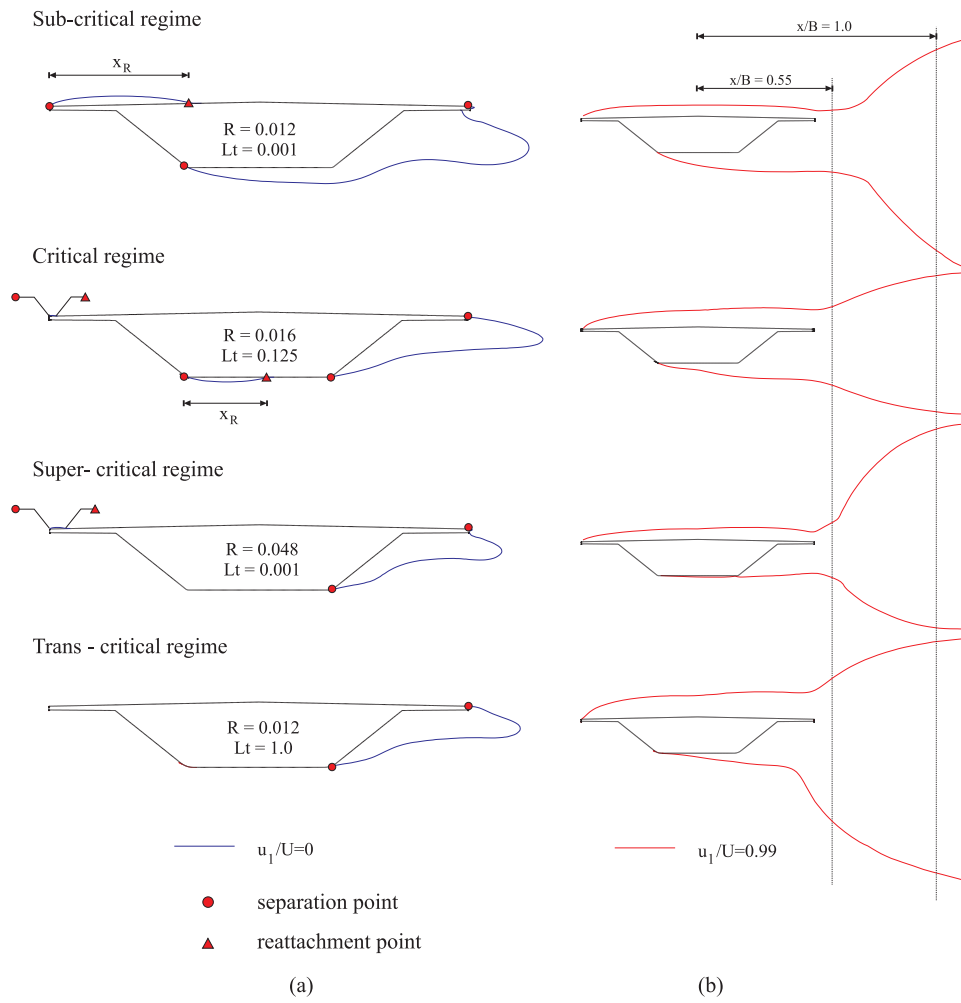


Figure 5: Aerodynamic regimes: null (a) and .99 (b) mean x-velocity isocontours

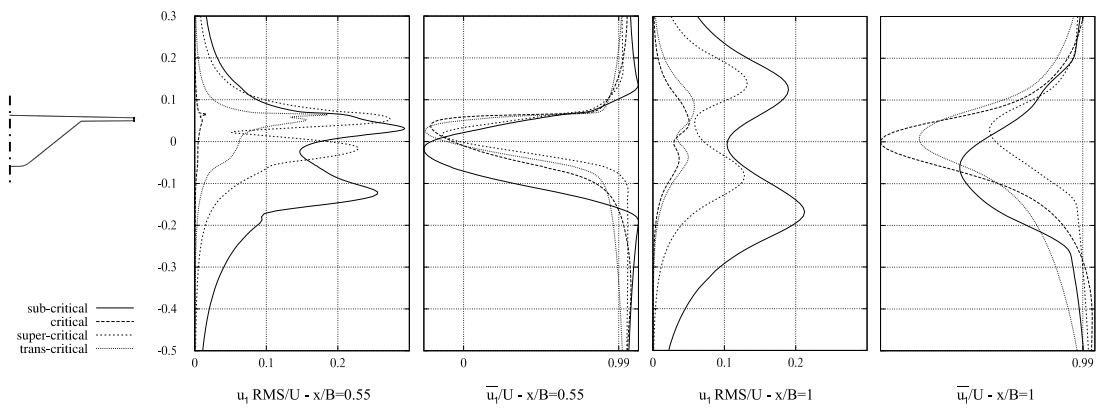


Figure 6: Mean (a) and RMS (b) horizontal velocity at  $x/B = 0.55$

The topological structure of the wake is obviously affected by the differences in the vortex shedding mechanism. Two-side vortex shedding in the sub and super-critical regimes gives rise to alternate vortices in the wake with opposite sign vorticity, even though dramatic differences exist in their characteristic size and vorticity concentration. One-side vortex shedding in the critical and trans-critical regimes gives rise to asymmetric wakes with vortices characterized by a small radius and low vorticity concentration.

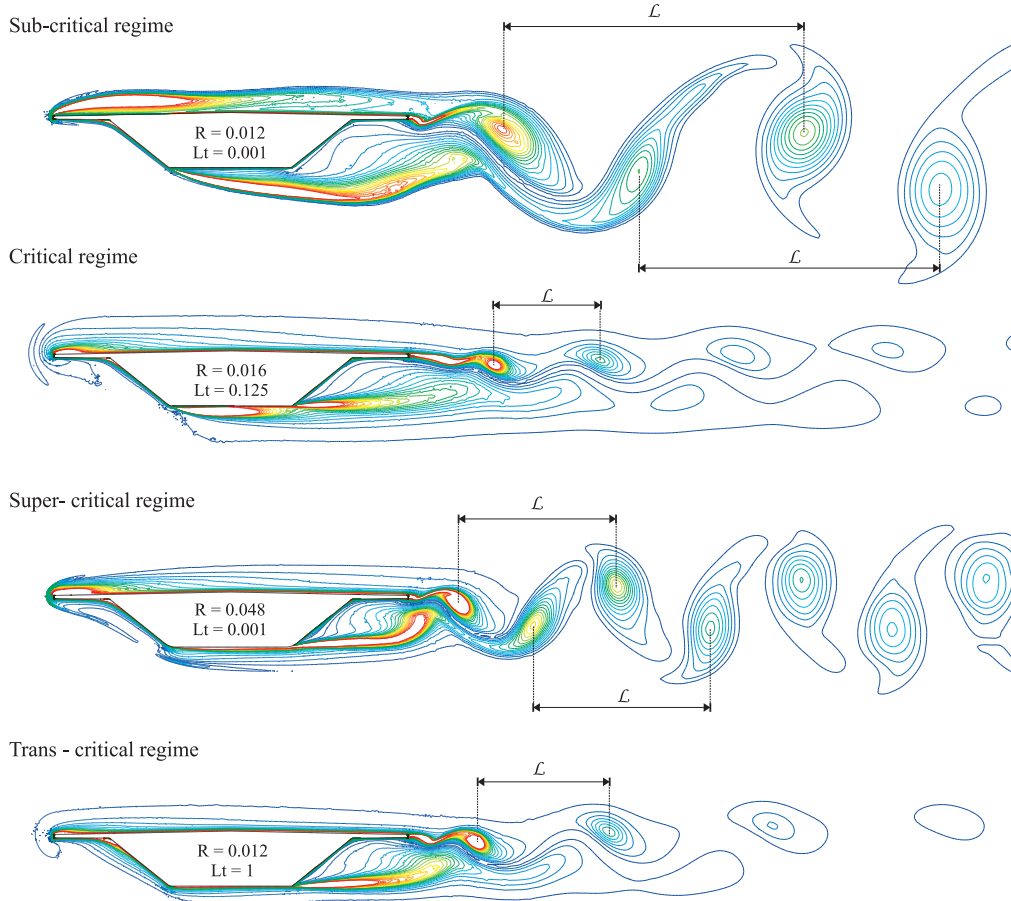
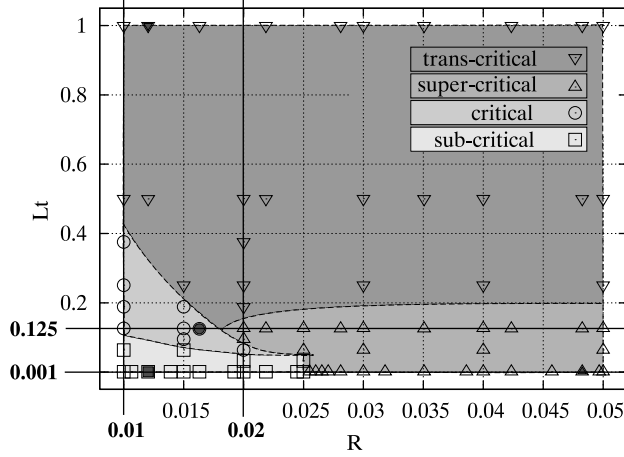


Figure 7: Aerodynamic regimes: instantaneous vorticity magnitude fields

### 3.3 Transition between regimes

Each point-wise simulation in the  $R - Lt$  plane previously shown in Figure 3 has been analyzed, looking at the boundary layer separation/reattachment and at the vortex shedding mechanism as the main classifying criteria. No other regimes have been recognized, so that each point-wise simulation has been ascribed to one of the four identified regimes. Figure 8 shows the resulting mapping of the  $R - Lt$  plane, with a selection of the analyzed set-ups. The black filled points refer to the specimen previously analyzed in depth.

The regime boundaries are tentatively sketched for the sake of clarity, even though their location is only approximately resolved in function of the point density in the  $R - Lt$  plane. Different kinds of transition occur at these boundaries, as already shown by the trend of the main integral parameters in Figure 4. A high rate of change characterizes the sub-critical and critical regimes, while smooth transitions occur between the super and trans-critical ones. The

Figure 8: Aerodynamic regimes in the  $R, Lt$  plane

high rate of change in the critical regime and its neighbourhood is of particular interest: the knowledge of the fluid flow phenomena that drive these abrupt variations is required first to point out some generalized features of the concerned regimes and second to suggest effective countermeasures during deck shape aerodynamic design. In order to do so, the upper and lower separation bubble length evolution is considered. The non-dimensional lengths  $x_R$  of the separation bubble at the upper and lower surfaces are scaled to the upper ( $B$ ) and lower ( $b$ ) flat plate  $x$ -lengths, respectively (see Figure 1 for notations). The length of the lower separation bubble in the sub-critical regime (fully separated flow) is defined as the distance along the  $x$ -axis between the separation point and the upper trailing edge. The reattachment points are evaluated looking at the  $x$ -wall tangential stress  $\tau_x$ , i.e.,  $x_R$  is defined as the distance from the separation point at which  $\tau_x$  changes sign from negative to positive. The non-dimensional lengths are plotted in Figure 9 versus the edge curvature radius  $R$  for two given  $Lt$  reference values, and versus the turbulence scale  $Lt$  for two given  $R$  reference values. The corresponding straights in the  $R - Lt$  plane are plotted in Figure 8.

The evolution across the sub-critical regime is mainly due to changes in the upper bubble length (square points in Figure 9(a)-(b)) because the boundary layer is completely separated on the lower horizontal plate (Figure 9(d)). The most significant variation of both the upper and lower bubble lengths can be observed between the sub-critical and critical regimes and across the latter: the reattachment of the boundary layer at the lower horizontal plate causes the sudden shortening of the upper bubble (Figure 9(b)); the progressive and significant shortening of the lower separation bubble for increasing  $R$  and  $Lt$  (see Figure 9(c) and (d) respectively) involves a further small decrease in the upper bubble length (Figure 9(b)). It is worth pointing out that a special case occurs at  $Lt = 0.001$ , where the lower bubble is not present for any  $R$  value, i.e., the separation point at the lower surface jumps downstream from the leading lower edge to the trailing one. In this case, the critical regime vanishes and a discontinuity occurs between the sub-critical regime and the super-critical one, as shown by the upper bubble trend in Figure 9(a). Generally speaking, the less extended the  $R$  and  $Lt$  range at which the lower bubble exists, the higher the rate of change in the critical regime, i.e. between the sub-critical and the super-critical regime. As a partial conclusion, the “on/off” nature of the lower bubble creation and its great sensitivity to the parameters mainly contribute to the abrupt changes in the sub-critical, critical and super-critical regimes at low  $Lt$  and  $R$  values.

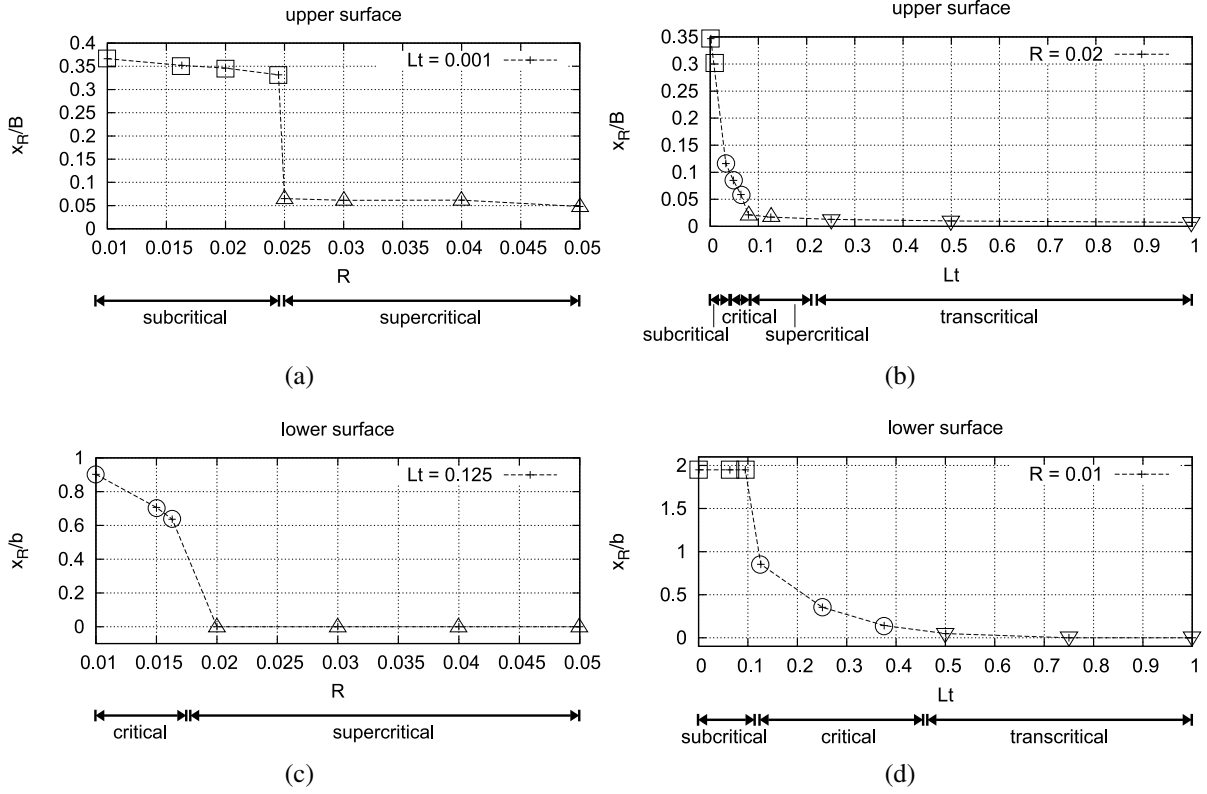


Figure 9: Length of the separation bubble

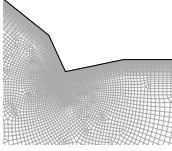

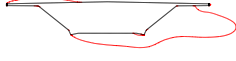

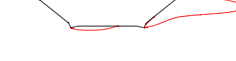
Finally, the separation bubbles at both the upper and lower surfaces show low or null  $R$  and  $Lt$  sensitivities along the super-critical and trans-critical regimes: the mean pressure distribution along the upwind canilever and the vortex shedding mechanism past the downwind one are confirmed as the main parameters that affect the smooth transition between these regimes.

#### 4 Application to an actual deck aerodynamic design

Bridge designers usually make an attempt to avoid deck shapes that are prone to changes in aerodynamic regimes in order to face well determined design wind loads. Hence, quasi-streamlined or bluff sections are preferred to the ones characterized by an intermediate degree-of-bluffness. Both streamlining and bluffness can be obtained, during the design phase or as a retrofitting measure, by means of aerodynamic appendages, e.g. rounded fairings, sharpening wedges and guide vanes, if the deck chord-to-width  $B/D$  and the upper-to-lower flat plate  $B/b$  ratios are imposed by structural needs. The aim of this section is to verify the effectiveness of some of these appendages, referring to the same deck section and the same incoming flow conditions investigated above. To do so, the Sunshine Bridge deck section with sharpening aerodynamic appendages at its lower edges (see Table 1), as tested in the wind tunnel by Ricciardelli and Hangan [11], is subjected to a sensitivity analysis to the turbulence length scale. The same previously explored  $Lt$  range ( $1e - 3 \leq Lt \leq 1$ ) is sampled with a coarse grid ( $\Delta \log(Lt) \approx 1$ ). The obtained results are summarized in Table 2.

The results clearly show that, even for the sharpest and the smoothest edge treatment, i.e., for the highest and smallest degree-of-bluffness, it is not possible to assure a unique aerodynamic

Table 2: Integral length scale sensitivity for the wind tunnel geometry

corner	inflow conditions	$St$	$\overline{C}_L$	$\overline{u}_1/U = 0$	regime
	$It = 1\%, Lt = 1e-3$	0.131	0.406		subcritical
	$It = 1\%, Lt = 1e-2$	0.131	0.333		subcritical
	$It = 1\%, Lt = 1e-1$	0.125	0.348		subcritical
	$It = 1\%, Lt = 1e-0$	steady	0.252		critical

regime at each turbulence scale.

The boundary layer at the lower surface is forced to separate by the leading edge sharpening at each length scale, so that the occurrence of the super-critical and trans-critical regimes is avoided. In the  $Lt \leq 0.1$  range, the sub-critical regime occurs analogously to what happens for the bare section, even though some peculiarities arise: the reattachment point is located along the trailing cantilever lower surface and the recirculation bubble at the upper surface grows to  $x_R/B \approx 0.5$  at the smallest length scale. On the contrary, at  $Lt = 1$ , the boundary layer at the lower surface reattaches to the horizontal plate so that the deck aerodynamics switches from the sub-critical regime to the critical one. In other words, from a designer's point of view, the introduction of sharpening appendages does not prevent the occurrence of two qualitatively different forms of aerodynamic behaviour, characterized by significant changes in wind loads.

The mean and rms pressure coefficient distribution around the deck with sharpening appendages at various  $Lt$  values are plotted in Figure 10 and compared with the Ricciardelli and Hangan [11] experimental data. The experimental data lie between the computational curves, and more precisely around the ones referring to  $0.01 \leq Lt \leq 0.1$ , which is supposed to be the  $Lt$  range generated in the wind tunnel by Ricciardelli and Hangan [11], except for the rms pressure coefficient distribution along the upper surface. In this case, the poor agreement can be ascribed to computational errors due to turbulence modelling or to the numerical approach, but the sensitivity to further small differences between the experimental and computational set-ups, e.g. in turbulence intensity, cannot be excluded *a priori*.

The obtained results suggest that the aerodynamic loads resulting from the so-called “smooth incoming flow” conditions, i.e. residual turbulence intensity and undefined turbulence length scale, should be handled with care because of non negligible uncertainty effects even for high or low deck degree-of-bluffness. The use of accurate evaluation of the turbulence intensity and a sensitivity analysis to the generated turbulence length scale seems to be proper method to guarantee a correct comparison of the results from different experimental facilities and to propose a wide range of wind load scenarios to designers. Finally, it is worth pointing out that, at least for this benchmark, the computational approach shows an analogous level of accuracy to the experimental one.

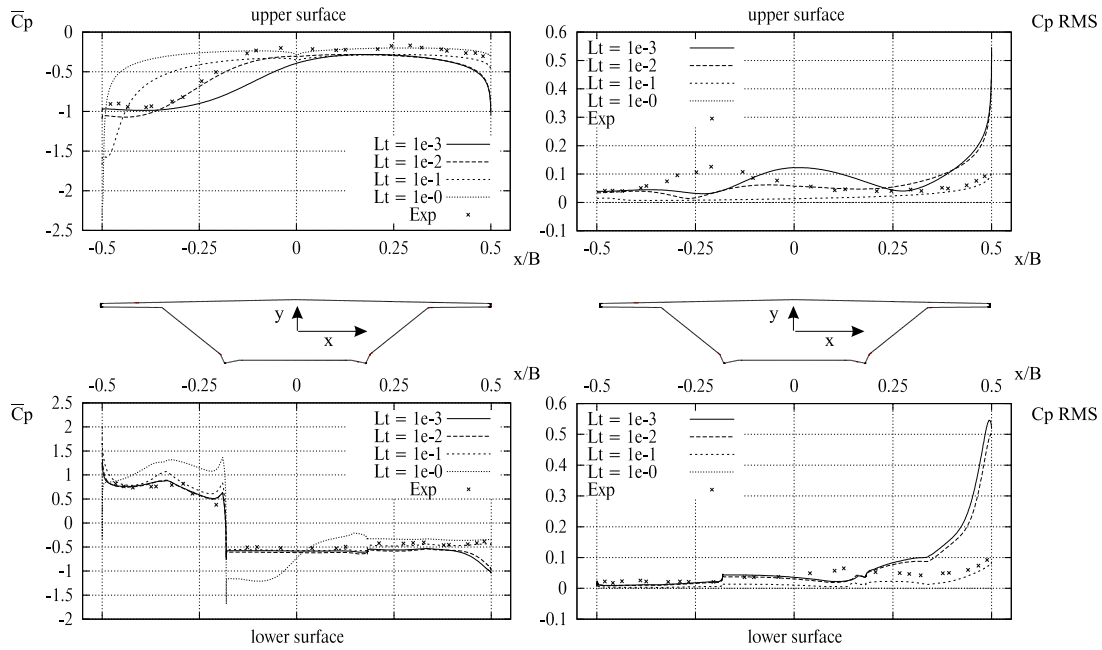


Figure 10: Mean and RMS pressure coefficient distribution for different inflow conditions - Sharpening appendages

## 5 Conclusions

In this paper, the edge degree-of-sharpness and free-stream turbulence scale effects on the aerodynamics of a trapezoidal bridge deck have been systematically addressed by means of a computational approach. The aerodynamic coefficients show a dramatic sensitivity to these parameters. The results have been analyzed in terms of mean and instantaneous flow fields, looking at both global and local fluid flow phenomena. The obtained results clearly confirm that the individual regimes proposed to classify the Reynolds number effects on bluff bodies can be further generalized to the aerodynamic effects of other set-up parameters, and characterized by the boundary layer separation and reattachment around a given bluff body. Furthermore, the results show that the shift from regime to regime can be driven not only by the overall incoming flow features, such as the Re number or the turbulence length scale, but also by local and small changes in the body shape. Finally, the sensitivity analysis to the turbulence scale has been applied to the actual extreme design solution obtained with sharpening aerodynamic appendages. Neither deck shape is capable of preventing switching from an aerodynamic regime to another one.

## Acknowledgements

The authors wish to thank Prof. F. Ricciardelli and Dr. C. Mannini for kindly providing the geometrical properties of the Sunshine Skyway Bridge and the wind-tunnel test set-up data. Further thanks go to Dr. S. Khris for the helpful discussions about the topics of the paper. The financial support provided by the Italian Ministry of Education, University and Research M.I.U.R. within the project “Aeroelastic phenomena and other dynamic interaction on non-conventional bridges and footbridges” is gratefully acknowledged.

**References**

- [1] H. Chen and V. Patel. Near-wall turbulence models for complex flows including separation. *AIAA Journal*, **26(6)**, 641–648, 1988.
- [2] N. K. Delany and N. E. Sorensen. Low-speed drag of cylinders of various shapes. *NACA TN 3038*, 1953.
- [3] D. Fransos and L. Bruno. Determination of the aeroelastic transfer functions for streamlined bodies by means of a navier-stokes solver. *Mathematical and Computer Modelling*, **43**, 506–529, 2006.
- [4] A. Laneville and C. Williams. The effects of intensity and large scale turbulence on the mean pressure and drag coefficients of 2d rectangular cylinders. Proc. 5<sup>th</sup> Int. Conference on Wind Effects on Building and Structures, Fort Collins, Colorado, July 8-14, 1979.
- [5] G. Larose and A. D’Auteuil. On the reynolds number sensitivity of the aerodynamics of bluff bodies with sharp edges. *Journal of Wind Engineering and Industrial Aerodynamics*, **94**, 365–376, 2006.
- [6] Q. Li and W. Melbourne. An experimental investigation of the effects of free-stream turbulence on streamwise surface pressures in separated and reattaching flows. *Journal of Wind Engineering and Industrial Aerodynamics*, **54/55**, 313–323, 1995.
- [7] C. Mannini. *Flutter Vulnerability Assessment of Flexible Bridges*. PhD thesis, University of Florence - Technische Universität Carolo-Wilhelmina zu Braunschweig, 2006.
- [8] C. Mannini. Personal communication. 2007.
- [9] C. Mannini, A. Soda, and R. Voß. Computational investigation of flow around bridge sections. pages 343–350, Dubrovnik, Croatia, 2006.
- [10] Y. Nakamura and S. Ozono. The effects of turbulence on a separated and reattaching flow. *Journal of Fluid Mechanics*, **178**, 477–490, 1987.
- [11] F. Ricciardelli and H. Hangan. Pressure distribution and aerodynamic forces on stationary box bridge sections. *Wind and Structures*, **4(5)**, 399–412, 2001.
- [12] A. Roshko. Experiments on the flow past a circular cylinder at very high reynolds number. *Journal of Fluid Mechanics*, **10**, 345–356, 1961.
- [13] G. Schewe. Reynolds-number effects in flow around more-or-less bluff bodies. *Journal of Wind Engineering and Industrial Aerodynamics*, **89**, 1267–1289, 2001.
- [14] G. Schewe and A. Larsen. Reynolds number effects in the flow around a bluff bridge deck cross section. *Journal of Wind Engineering and Industrial Aerodynamics*, **74-76**, 829—838, 1998.
- [15] T. Tamura and T. Miyagi. The effect of turbulence on aerodynamic forces on a square cylinder with various corner shapes. *Journal of Wind Engineering and Industrial Aerodynamics*, **83**, 135–145, 1999.
- [16] D. Wilcox. *Turbulence Modelling for CFD*. DCW Industries Inc., La Cañada, California, 1998.